



science.sciencemag.org/content/365/6456/926/suppl/DC1

**Supplementary Materials for
Solar System chaos and the Paleocene–Eocene boundary age
constrained by geology and astronomy**

Richard E. Zeebe* and Lucas J. Lourens

*Corresponding author. Email: zeebe@soest.hawaii.edu

Published 30 August 2019, *Science* **365**, 926 (2019)
DOI: 10.1126/science.aax0612

This PDF file includes:

Materials and Methods
Supplementary Text
Figs. S1 to S8
Tables S1 to S3
References

Materials and Methods

Data analysis. Sediment core material at ODP Site 1262 was recovered during ODP Leg 208 on the Walvis Ridge (southeastern Atlantic Ocean), with Site 1262 being the deepest site of a depth transect (P/E paleo-water depth $\sim 3,600$ m) (7, 16, 36). The section ~ 170 - 110 m at Site 1262 includes the PETM and ETM2, with the Elmo horizon (7) only designating the red clay layer (<40 -wt% CaCO_3), coinciding with ETM2 peak warmth (full ETM2 duration is ~ 60 - 80 kyr). The a^* record from Site 1262 was linearly interpolated to an equally spaced grid, demeaned, and linearly detrended in the depth domain (Norm. a^* , Fig. 1). Spectral analysis of the record in the interval between (and excluding) the PETM and ETM2 ($\Delta z \simeq 2.1$ cm) using the multitaper and Blackman-Tukey methods and Fast Fourier Transform yielded dominant long periods of ~ 5.1 m and ~ 1.25 m (frequencies, f 's, of ~ 0.2 and ~ 0.8 cycles m^{-1} , Fig. S5), equated to long and short eccentricity cycles. The long cycle's frequency can be refined to 0.196 m^{-1} *a posteriori* (see below). Next a Gaussian filter was applied to extract the low frequency components. For clarity, a narrow filter was used ($f = [0.196 \text{ } 0.80] \text{ m}^{-1} \pm 20\%$, Fig. 1), which also gives the correct number of short cycles ($n = 18$) between (and excluding) PETM and ETM2 (though counting ETM2 as $n = 1$, see Fig. S3) (8). However, the analysis also works with a wider filter (our chronology is based on the long cycle, see below), only the short and long cycles in the filter output appear less distinct. Once a time-depth relationship has been derived (below), the sum of the above filter outputs in the time domain represents the data target a^{**} for comparison with Earth's orbital eccentricity as computed by astronomical solutions (Fig. 1). For the final ~ 5 -Myr record ($\Delta z \simeq 2.4$ cm), a long period of 0.196 m^{-1} provided the best fit with the solutions ZB18a and La10c with the smallest RMSDs (see [main manuscript](#) and Table 1).

Floating chronology. Based on the number of long cycles in the data target ($N \simeq 12$, equated to long eccentricity cycles), the total length (L) of the record including

PETM and ETM2 represents about 5 Myr (T) in the time domain, with an average sedimentation rate of $\sim 1.26 \text{ cm kyr}^{-1}$, in agreement with earlier work (7, 8, 10):

$$r_{sed} = L/T = NP'/(NP) = P'/P, \quad (1)$$

where $P' = 5.10 \text{ m}$, and $P = 405 \text{ kyr}$ are the periods in depth and time domain. A slightly higher, optimized sedimentation rate of $\sim 1.32 \text{ cm kyr}^{-1}$ was reported for the interval between PETM and ETM2 only (14, 35). Assuming, for simplicity, a uniform sedimentation rate throughout the section provides a first-order floating chronology for the record. Importantly, for the present analysis, it is unnecessary to anchor the data record to an absolute precise age *a priori*. It suffices to assume that Elmo's absolute age falls somewhere within a long eccentricity cycle around 54 Ma (i.e., is not offset by one or more 405-kyr cycles, see below). Absolute ages is one final result of our analysis (see [main manuscript](#)).

Age of ETM2/Elmo. There is consensus within the cyclostratigraphic community on the tuning of the 18 statistically identified hyperthermal events from 50 Ma to ETM2/Elmo, using the stable 405 kyr eccentricity cycle (see Fig. 2 in ref. (37), ref. (38), and references therein). This gives a very precise age for ETM2/Elmo, likely within 1-2 precession cycles, i.e., less than a short eccentricity cycle and hence more precise than our requirement for the present study, as we only assume that Elmo falls somewhere within a long eccentricity cycle around 54 Ma (i.e., $\pm 200 \text{ kyr}$). Our initial allowance of $\pm 200 \text{ kyr}$ is thus larger than the range of uncertainties from cyclostratigraphy. Our astronomically calibrated age model (Fig. S8, Table S3) then gives a final age of 54.05 Ma for Elmo, which agrees exactly with the most recent age determined independently (27).

Age and time scale errors. The P/E boundary age t_A (56.01 Ma, tie point A, Fig. S6) is determined by propagating the depth z_A through our optimization routine with steps: PETM stretch (k), floating chronology, time shift (τ), i.e.,

$z_A \rightarrow z'_A \rightarrow t'_A \rightarrow t'_A + \tau = t_A$, repeat to find $\min[\text{RMSD}(k, \tau)]$. The effect of the following parameter changes on our calculated t_A (after re-optimization) are small: increasing filter width to $\pm 50\%$ (0 kyr), swap ZB18a for La10c (2 kyr), uncrop PETM (7 kyr), shifting z_A by ± 4 data points (4 kyr). Mathematically, our optimization routine determines k and τ to within one grid point, with error \lesssim grid spacing and hence \lesssim data resolution (2 kyr). Including 3 data points below point A in the PETM stretch that are possibly affected by dissolution (Fig. S6) shifts t_A by -12 kyr. Variations in the long-term sedimentation rate ($\gtrsim 500$ kyr) translate to $t_A \pm \sim 15$ kyr (see PETM duration below). Potentially larger errors arise from the $g_2 - g_5$ frequency (g_{25}) assumed constant at 405 kyr in our age model. Theoretical and observational evidence suggests exceptional stability of g_{25} (5, 6, 8). However, across certain intervals g_{25} changes slightly. In ZB18a, its argument (6) Θ_{25} changes by ~ 0.9 rad between 60 and 50 Ma (Fig. S7). $\Delta\Theta_{25} = 2\pi$ corresponds to a full period $P = 405$ kyr and hence the time offset is $\Delta_t = P \cdot \Delta\Theta_{25}/2\pi \simeq 58$ kyr. Spectral analysis indicated changes in g_2 and g_5 by $x_2 \simeq -0.2\%$ and $x_5 \simeq +0.02\%$ within this 10-Myr window, yielding a time offset:

$$\Delta_t = \Delta T [g_{25} / (g_2 \delta_2 - g_5 \delta_5) - 1] \simeq 50 \text{ kyr} , \quad (2)$$

where $\Delta T = 10$ Myr and $\delta_i = 1 + x_i/100$, consistent with the offset from $\Delta\Theta_{25}$ above. Eq. (2) follows from $\Delta_t = \Delta T' - \Delta T = N(P' - P) = \Delta T(f/f' - 1)$, where Δ_t is the time offset of a periodic function with periods P, P' and frequencies f, f' after N cycles. Δ_t estimates the error between the astronomical solution and an age model that equates the uncorrected long eccentricity data cycle to an exact 405-kyr cycle. Because we corrected the data cycle's period *a posteriori* (see above), our $\Delta_t \lesssim 50$ kyr. **PETM duration.** The PETM duration t_{AF} (170 kyr, tie point A to recovery inflection point F, Fig. S6) is determined by propagating the depths z_A and z_F through our optimization routine, including the PETM stretch (see above). Briefly, the match

of all cycles in a^* below and above the PETM interval relative to our astronomical solution reveals how much time must be represented across the PETM interval, i.e., how many PETM grid points (k) need to be stretched to obtain a meaningful fit. (A similar approach was recently developed independently (15)). In other words, the reduction/gap in carbonate sedimentation across the PETM is determined by the entire record, except the PETM itself. The overall, multimillion-year sedimentation rate (r_{sed}) is thus critical for the optimized fit to the astronomical solution over 5 Myr (Fig. 1), not r_{sed} across the PETM, which is affected by dissolution, erosion, and possibly changes in terrigenous input (see [main manuscript](#)). For our first-order floating chronology, we used a uniform r_{sed} . However, long-term r_{sed} (excluding PETM and ETM2) was slightly higher during some intervals and lower during others, at the same overall r_{sed} (see refs. (8, 10) and Fig. S8). Variability in r_{sed} can be assessed via its standard deviation from our final age model, $\sigma \simeq 0.04 \text{ cm kyr}^{-1}$ for roughly 500-kyr intervals (excluding PETM and ETM2, Fig. S8). Thus, if r_{sed} for the 500-kyr intervals (Δ 's) just below and above the PETM were within $r_{sed} \pm \sigma$, then the error in t_{AF} is $2\Delta[1 - r_{sed}/(r_{sed} \pm \sigma)] \simeq \pm 30 \text{ kyr}$. This derives from $\Delta'/\Delta = (z/r_{sed}')/(z/r_{sed})$, where z is the corresponding depth interval; factor 2 is for 2 intervals (below and above PETM). Errors from uncertainties in the assignment of tie points A and F, say $\pm 2 \text{ cm}$ (Fig. S6) on t_{AF} is small ($\pm 2 \text{ kr}$) because the uncertainty is much smaller than the total stretched interval length ($> 2 \text{ m}$). Mathematically, our optimization routine determines the PETM stretch (k) to within one grid point, with error \lesssim grid spacing and hence \lesssim data resolution (2 kyr).

Between points A and F ($\sim 0.7 \text{ m}$, Fig. S6) r_{sed} was reduced relative to pre-PETM levels but gradually increased to ~ 1.5 -2 times pre-PETM levels between F and G at Sites 1263 and 1266 (20, 21). Using a 1.5-fold rise in r_{sed} , the total PETM duration then is $t_{AG} \gtrsim 200 \text{ kyr}$. The uncertainty in t_{AG} is larger than in t_{AF} , hence we only estimate a lower bound for t_{AG} . Furthermore, our duration t_{AF} (see above) might

be an underestimate, given higher recovery sedimentation rates, as compacting the recovery interval would require additional stretching of the main phase.

Alternatively, instead of a reduction/gap of carbonate sedimentation across the PETM main phase, could erosion of Paleocene (pre-PETM) sediment account for the bulk of the ~ 16 cm clay layer (< 1 -wt% CaCO_3) and hence for the offset of \sim one short eccentricity cycle between the 1262 record and the astronomical solution? PETM sediment modeling (22) suggests erosion of the total sediment column by ~ 21 cm at Site 1262, corresponding to a ~ 2.5 cm residual clay layer (at 88% initial CaCO_3 dry weight and constant porosity). This is consistent with tie point A (PETM onset) being located ~ 3 cm above the clay layer base at Site 1262 (ref. 20, Fig. S6). At an average r_{sed} , 21 cm of sediment represent ~ 17 kyr. Thus, at Site 1262 erosion of Paleocene sediment alone may account for \sim one eroded cycle in precession, but not in short eccentricity.

Astronomical Solutions. Solar system integrations were performed following our earlier work (6, 23, 24) with the integrator package HNBODY (39) (v1.0.10) using the symplectic integrator and Jacobi coordinates (23, 40). All simulations include contributions from general relativity, available in HNBODY as Post-Newtonian effects due to the dominant mass. The Earth-Moon system was modeled as a gravitational quadrupole (41) (lunar option), shown to be consistent with expensive Bulirsch-Stoer integrations up to 63 Ma (6). Initial conditions for the positions and velocities of the planets and Pluto were generated from the DE431 ephemeris (42) using the SPICE toolkit for Matlab. The integrations for ZB18a (ZB = Zeebe-HNBODY) included 10 asteroids, with initial conditions generated at ssd.jpl.nasa.gov/x/spk.html. The 10 asteroids were treated as heavyweight particles in HNBODY, subject to the same full interactions as the planets. Coordinates were obtained at JD2451545.0 in the ECLIPJ2000 reference frame and subsequently rotated to account for the solar quadrupole moment (J_2) alignment with the solar rotation axis (6). Our new solution

ZB18a features a specific combination of J_2 and number of asteroids (see Section S6). Interestingly, it appears that parameters required for long-term integrations compatible with geologic observations of the past are not fully compatible with our best knowledge of the current solar system (see Section S6). Earth's orbital eccentricity and inclination from ZB18a is available at www2.hawaii.edu/~zeebe/Astro.html and www.ncdc.noaa.gov/paleo/study/26970. We provide results from 100-0 Ma but caution that the interval 100-58 Ma is unconstrained due to chaos.

Supplementary Text

S1 Lyapunov exponent

Positive Lyapunov exponents describe the rate of exponential divergence of nearby trajectories from perturbed initial conditions, corresponding to a chaotic region. With respect to the chaotic behavior of the solar system, Lyapunov exponents characterize the sensitivity of orbital solutions to initial positions and velocities. Small differences in initial conditions grow exponentially, with a time constant (Lyapunov time) for the inner planets of only ~ 5 Myr, e.g., refs. (4, 12, 43). For example, a difference in initial coordinates of 1 mm grows to ~ 1 AU after 163 Myr (6). Thus, the chaotic nature of the planetary orbits makes it fundamentally impossible to predict their evolution accurately beyond a time scale of order $\sim 10^8$ years.

S2 Cretaceous resonance transition (Libsack record)

Geologic evidence was recently presented for a chaotic resonance transition in a Cretaceous record from the Western Interior Basin (Libsack record) (9, 44). Here we evaluate potential constraints from the Libsack record on astronomical solutions in general, and on our solution ZB18a specifically. First, constraining astronomical solutions for ages as old as, say, 80 Ma is inherently difficult. Due to the chaotic

nature of the system, the solutions are highly sensitive to initial conditions/small perturbations and start to diverge around 50 Ma (divergence time τ , see Section S6), which fundamentally precludes identifying a unique solution for ages much older than τ . For example, differences in Earth's initial position of only 1×10^{-16} au (many orders of magnitude below measurement errors) leads to two completely different solutions around 80 Ma (6). As a result, a vast number of solutions can be generated that agree up to ~ 60 Ma (and agree with ZB18a, if desired) but completely disagree at 80 Ma (6). Importantly, all those solutions would fit the a^* -1262 record equally well (58-53 Ma) but may show entirely different resonance transitions during the Cretaceous period, or none at all.

Ma et al. (9) tested a few astronomical solutions and concluded that La04 (5)[†] yielded a better fit to their geological data than La10d and La11 (for solution labels, see Table 1, [main manuscript](#)). However, Ma et al. also noted that the Libsack short eccentricity amplitude modulation was anti-phased with La04 throughout most of the record (see Fig. S1c,d). To probe the likelihood of finding a solution that fits both the a^* -1262 record (58-53 Ma) and the Libsack record (90-83 Ma), we ran an ensemble of test simulations ($N = 80$) with small successive offsets in Earth's initial position ($\Delta r_i = 1.25 \times 10^{-11}$ au in radial distance, solution tags ZB18a.x). Otherwise the simulations used the same setup as ZB18a, except for a 6-day timestep (Δt) instead of 2 days. The difference in the solutions for $\Delta t = 6$ d vs. 2 d was negligible up to 60 Ma (see also ref. 6). We emphasize that our ensemble test is not an attempt to identify a unique solution that would be valid to, say, 90 Ma. Rather, we illustrate that such an attempt is likely quixotic without suitable continuous geologic records that connect the a^* -1262 and the Libsack record, i.e., closes the gap between ~ 83 and ~ 58 Ma.

[†]More recent solutions (6) agree with one another to ~ 50 Ma including La10x but collectively disagree with La04 already beyond ~ 41 Ma; La04 may hence be considered outdated.

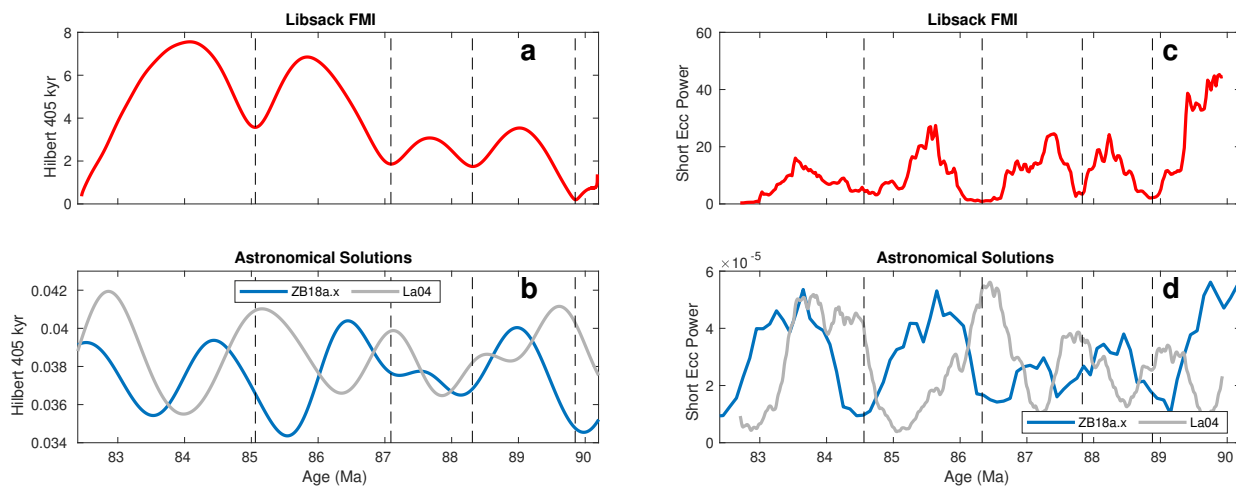


Figure S1. Comparison of Libsack record (9) and astronomical solution ZB18a.x, where $x = 56$ (see text) and La04 (5). FMI (Formation Micro-resistivity Imaging) is a carbonate content proxy (9). For details on Hilbert transform and short eccentricity power, see text and R-scripts provided in ref. 9.

Several of the 80 solutions showed a resonance transition within the interval 90-83 Ma, similar to the one suggested by the Libsack record. For example, the 405-kyr Hilbert transform of Earth's eccentricity for solution ZB18a.56 indicates a transition from ~ 1 Ma to ~ 2 Ma periodicity from 88 to 83 Ma (Fig. S1b), which is confirmed by the short eccentricity amplitude modulation (Fig. S1d). The agreement with the Libsack record is modest for the Hilbert transform but good for the phase of the short eccentricity power (except for the amplitude around 84 Ma). The match/mismatch may also be expressed quantitatively using the root mean square deviation (RMSD) between record and solution after normalization (Table S1), although the RMSD is a crude measure in this case. Most importantly, however, striving for maximum agreement between data record and solution is not the point here. Critical is that several out of only 80 test solutions show similar or better agreement than, for instance, La04 (for examples, see Table S1). It follows that given the vast number of possible initial conditions, a large number of solutions can be generated that will match the a^* -1262 and the Libsack record within data uncertainty (cf. ref. 6). Hence

Table S1. RMSD^a between Libsack record and selected astronomical solutions.^b

	La04	ZB18a.56	ZB18a.77
Hilbert ^c	1.7214	1.4017	1.2834
Short Ecc AM ^c	1.5968	0.9899	1.2282

^aRoot mean square deviation.

^bRecord and solution were demeaned and normalized to their standard deviation before calculating RMSD.

^c405-kyr Hilbert transform/power in short eccentricity amplitude modulation of FMI (Libsack) and Earth's eccentricity (solutions), see text.

at present, the Libsack record in isolation does not provide a constraint to identify a unique astronomical solution, valid to, say, 90 Ma.

The situation is different for the a^* -1262 record from 58 to 53 Ma because the age window is very close to τ . This directly connects the time interval of geological observation to the interval over which astronomical solutions start to diverge (see [main manuscript](#)). Thus, no large unconstrained gap exists as in the case of the Libsack record (83 – 58 = 25 Ma), during which chaos can drive the solutions apart. To advance the field, suitable continuous geologic records are required that connect, for instance, the a^* -1262 and the Libsack record. In other words, records are needed that close the gap between ~ 83 and ~ 58 Ma and exhibit distinct patterns for testing astronomical solutions.

S3 Precession, eccentricity, and sedimentation rates

Precession vs. eccentricity consistency check. The power spectrum of the a^* -1262 record shows that the three main precession and eccentricity components occur as their expected ratios. For example, given $g_2 \simeq 1/174$ kyr, $g_4 \simeq 1/72$ kyr, $g_5 \simeq 1/304$ kyr, $E_1 = 1/(g_2 - g_5) = 405$ kyr, $E_2 = 1/(g_4 - g_2) = 124$ kyr, $E_3 = 1/(g_4 - g_5) = 95$ kyr, and precession motion $\Psi = 25.675$ kyr, then

$1/(\Psi^{-1} + g_i^{-1})$ gives $P_1 = 23.690$ kyr, $P_2 = 22.385$ kyr, $P_3 = 18.956$ kyr and one can derive that $E_1^{-1} = 1/P_2 - 1/P_1$, $E_2^{-1} = 1/P_2 - 1/P_3$, and $E_3^{-1} = 1/P_3 - 1/P_1$. The results of our spectral analysis in the depth domain suggest that $E_1 \simeq 5.10$ m, $E_2 \simeq 1.70$ m and $E_3 \simeq 1.25$ m, and $P_1 \simeq 30.5$ cm, $P_2 \simeq 29.0$ cm, and $P_3 \simeq 24.5$ cm. Now if we derive E_1 , E_2 and E_3 from these P_1 , P_2 and P_3 as above, it gives values of 5.90, 1.58 and 1.25 m, respectively. This is within errors, given that the 405 kyr component of eccentricity (E_1) is only represented by ~ 4.5 cycles within the studied interval between the PETM and ETM2 and has therefore relatively large error bars. Moreover, a small change of, e.g., plus and minus 0.1 cm in P_1 and P_2 would drop the derived E_1 by 70 cm. This suggests that notwithstanding small changes in sedimentation rates, the precession and eccentricity pacing is in accord with the theoretical forcing.

Estimating early Eocene precession periods? The accuracy of the following assessment is probably low, as the uncertainties involved are estimated to be large. However, it may be instructive to ask if one can estimate (and evaluate the consistency of) precession periods in the time domain during the early Eocene from our results. To maximize the chances for obtaining a clean and undistorted orbital forcing signal (including the precession band), we focus here on the interval between (and excluding) the PETM and Elmo (PELMI for short). Moreover, we will also trim short segments at the edges that might have been affected by these two events, i.e., we will use the section 137.50-117.57 m (from tie point E1 to below the Elmo horizon, see Fig. S8, Table S3).

At least two important issues warrant attention here. (1) Our initial age model is based on the long eccentricity cycle g_{25} , assumed constant at 405 kyr. However, g_{25} is generally slowly changing in the astronomical solutions before 50 Ma, i.e., precisely across the PELMI (Fig. S7). Thus, we have to consider that in reality, the long eccentricity forcing period may have been different from a constant 405-kyr cycle across certain intervals. For example, in our solution ZB18a, $g_{25} \simeq 401$ kyr

during the PELMI (though these estimated periods from spectral analysis have large uncertainties, given that the interval length is <2 Myr). Thus, the total duration of an interval (and possibly the number of precession cycles within) should not be estimated assuming a constant 405-kyr cycle as in our initial age model. Rather, we will determine durations based on tuning to our solution ZB18a. (2) Even when using the solution, we found that employing an averaged, constant r_{sed} is insufficient to properly determine precession periods and frequencies, as even small changes in r_{sed} lead to important shifts in the position of the precession peaks in the power spectrum. Thus, we use our final, tuned age model (Fig. S8, Table S3) and spectral analysis of the tuned record in the time domain to estimate precession periods across the PELMI.

The final result for the periods is given as ranges, using the Rayleigh frequency ($f_R = 6.4 \times 10^{-4} \text{ kyr}^{-1}$) as a rough guide for errors in estimating frequencies from peaks in the power spectrum: $P_1 = 23.7 - 24.5 \text{ kyr}$, $P_2 = 21.6 - 22.2 \text{ kyr}$, and $P_3 = 18.5 - 18.9 \text{ kyr}$. Given additional uncertainties in data and solution, we consider these values essentially indistinguishable within errors from the P_i values of ~ 23.69 , 22.39 , and 18.96 kyr for the past 20 Myr. We note that our final tuned sedimentation rate averaged over the PELMI as defined above is $r_{sed} \simeq 1.28 \text{ cm kyr}^{-1}$. This is closer to, but still smaller than, the most recent TimeOptMCMC value of 1.32 cm kyr^{-1} for nearly the same interval (35). The ranges for P_1 , P_2 , and P_3 given in ref. (35) are different from ours but overlap within their 2σ error bounds.

S4 Comparison with TimeOpt analysis

Below we provide a comparison with TimeOpt and TimeOptMCMC analyses of the a^* -1262 record within the PETM-ELMO interval (Meyers, 2015; Meyers and Malinverno, 2018; Meyers, 2019; M15, MM18, and M19 hereafter) (14, 15, 35). We emphasize, however, that this comparison only concerns the section analyzed in Meyers' work, i.e., the PETM-Elmo interval (PELMI, ~ 55.8 -54 Ma, which is

Table S2. Comparison of $g_4 - g_3$ from ZB18a and TimeOpt^a analysis of a^* -1262.

	Interval	g_3	g_3	g_4	g_4	$g_4 - g_3$
	(Ma)	(" / yr)	(kyr)	(" / yr)	(kyr)	(Myr)
ZB18a	20-0	17.3695	74,613	17.9184	72,328	2.362
ZB18a	56-54	17.2678	75,053	18.1428	71,433	1.481
MM18 ^b	~56-54	17.4808	74,139	18.3483	70,633	1.494

^aSee refs. (14, 35).

^bRef. (35).

not our focus), and not the full record from 58-53 Ma used in our analysis. Our conclusions remain unchanged because they are based on the full record from 58-53 Ma, our final age model, and our astronomical solution ZB18a. Importantly, our and the TimeOptMCMC approach are fundamentally different. Our approach starts with the computation of astronomical solutions based on solar system physics; TimeOptMCMC does not use solar system integrations. Also note that due to the chaotic nature of the solar system, even large ensemble integrations of orbital solutions with our approach do not lead to error statistics for comparison with, e.g., MM18's TimeOptMCMC output (see Section S7).

Changes in $g_4 - g_3$. An independent analysis of the a^* -1262 record was recently provided (35), using an updated version of their time scale optimization routine TimeOpt (14) to reconstruct g 's (TimeOptMCMC). Stunningly, they reconstructed $g_4 - g_3 \simeq 1.5$ Myr within the interval ~56-54 Ma, which matches ZB18a prior to ~50 Ma. However, spectral analysis of our solution ZB18a shows that the individual g -values from ZB18a and from TimeOptMCMC (35) are different (see Table S2). In ZB18a, the g_3 frequency drops within PELMI relative to 0-20 Ma, whereas MM18's g_3 frequency increases. Regarding uncertainties, the values for g_3 and g_4 from ZB18a are outside the 1σ error bounds given by MM18, but within 2σ . Note that the g -values

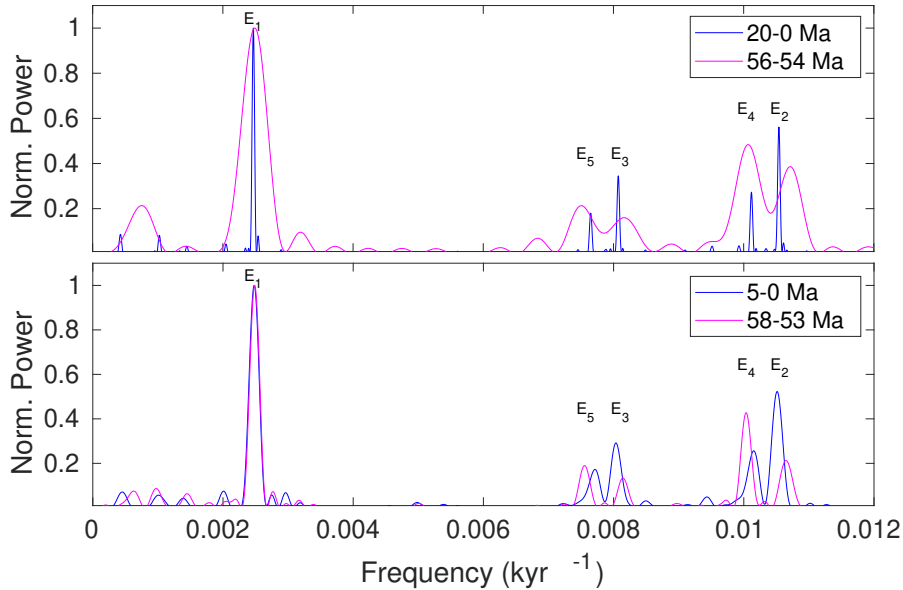


Figure S2. Fast Fourier Transform (FFT) spectra of Earth’s orbital eccentricity from ZB18a for different time windows. The windows 56-54 Ma and 58-53 Ma roughly correspond to the PETM-ELMO interval and the full interval of our a^* -1262 analysis, respectively. The windows 20-0 Ma and 5-0 Ma allow comparison to more recent values. Note the changes in the amplitudes and positions of E_2 to E_5 .

from, say, Laskar et al.’s solution La10c (33) and ZB18a are very similar from 56-54 Ma (not shown).

Sedimentation rates. Interestingly, MM18 found values for $E_2 = 91.975$ kyr and $E_3 = 118.946$ kyr for the PELMI with TimeOptMCMC, which are considerably smaller than the present-day values of ~ 95 and ~ 124 kyr, respectively. The power spectrum of ZB18a, our optimal astronomical solution, shows that the amplitudes of E_2 and E_3 are reduced between 56 and 54 Ma, relative to the past 20 Myr (see Fig. S2), but that their period is only slightly smaller, i.e., $E_2 \simeq 93$ kyr and $E_3 \simeq 122$ kyr. Our value for E_2 is close to the 1σ error bound given by MM18, but our value for E_3 is outside the 2σ bound. Hence, overall the change in these periods in ZB18a is smaller than suggested by MM18. If one would consider a lower sedimentation rate of 1.28 cm kyr^{-1} (this

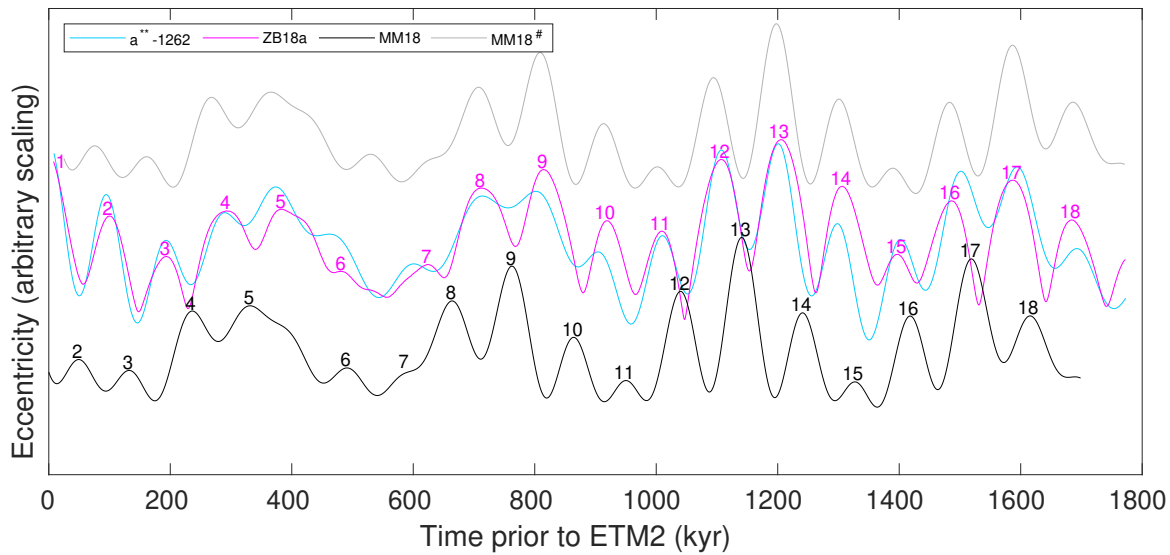


Figure S3. Eccentricity from cyclostratigraphy and astronomical solution ZB18a (magenta) across the PETM-ELMO interval, excluding the PETM. Cyan: a^{**} -1262 from our data analysis; black: MM18 eccentricity model from TimeOptMCMC (35); gray: MM18’s time axis $\times(1.316/1.28)$ and aligned with cycle 18 of ZB18a (MM18#).

study) instead of $1.316 \text{ cm kyr}^{-1}$ (MM18), one can estimate periods ($\times 1.316/1.28$) for MM18’s E_2 and E_3 of 94.6 and 122.3 kyr, respectively, i.e., closer to our solution ZB18a and the ratios between E and P components (see consistency check above).

The difference between Meyers’ (14, 15, 35) and our average sedimentation rate estimates also gave rise to different numbers of short-term eccentricity cycles for the PELMI in the original TimeOpt analysis (14). The recent results from TimeOptMCMC (35) appear more in line with ours, except sedimentation rates are still different (Fig. S3). We detected 18 short-term eccentricity cycles in the a^{*} -1262 record (counting ETM2 as $n = 1$, see Fig. S3), which also agrees with the analysis of Westerhold et al. (2007), who additionally used Fe intensities as an independent proxy (8). The critical part of the cycle analysis concerns the interval ~ 500 kyr prior to ETM2/Elmo, where the expression of precession and eccentricity is reduced due to the minimum in the long eccentricity cycle (“very long eccentricity node”, see Fig. S3, and discussion and

Fig. 5 in ref. (8)). In this interval, the ZB18a solution shows an aberrant short-term eccentricity pattern between cycle numbers 5 and 8, due to the fact that the E_2 ($\simeq 93$ kyr) and E_4 ($\simeq 100$ kyr) (Fig. S2) are almost anti-phased. This interference pattern gives rise to an overall reduced eccentricity signature and a prolonged short-term eccentricity, i.e., a relatively longer time interval between cycles 6 and 7 (magenta labels, Fig. S3).

In summary, irrespective of any internal changes in sedimentation rates (see Figure 18d of M19), MM18 arrived at a total PELMI duration of 1699 kyr, assuming total length = 22.4 m and an average sedimentation rate of 1.32 cm kyr^{-1} (Fig. S3). We arrive at a total duration of 1758 kyr for this interval based on our tuning after re-optimization. Our tuning implies an average sedimentation rate of 1.27 cm kyr^{-1} (this value may be increased to $\sim 1.28 \text{ cm kyr}^{-1}$ for a slightly trimmed interval, see above). If we stretch MM18's time axis by the ratio of sedimentation rates ($\times 1.316/1.28$) and align cycle 18 of MM18 and ZB18a, then MM18's reconstructed eccentricity agrees quite well with our astronomical solution (Fig. S3). In addition, note that the TimeOpt envelope regression model (Eq. (1) in M15) identifies a maximum r^2 -envelope at a sedimentation rate of 1.28 cm kyr^{-1} , i.e., closer to our value. Moreover, the spectral power fit (r^2 -spectral; dark gray line, Figure 3e in M15) shows two peaks with high r^2 values.

S5 P/E boundary relative to K/T boundary

Hilgen et al. (28) suggested that the entire Paleocene comprises twenty-five 405-kyr cycles. Using radiometric age constraints for the K/T boundary, they estimated an age of about 56 Ma for the P/E boundary (PEB). However, no error bounds were provided and the cycle-age conversion was based on the now outdated solution La04 (5, 6) (see above). Hilgen et al. also noted that "... an alternative 405-kyr younger or, less likely, older tuning cannot be excluded ...". Taking La04's 405-kyr

maximum around 56 Ma as Hilgen et al.'s estimated PEB age yields 56.07 Ma. This is older than, and falls outside the errors of, our PEB age of 56.01 ± 0.05 Ma.

S6 Parameters of astronomical solutions

Our new astronomical solution ZB18a is part of a certain type (class) of solutions that can be generated using certain sets of parameters such as a combination of the solar quadrupole moment (J_2) and number of asteroids (N) included in the computation (6). For example, ZB18a was generated with a low $J_2 = 1.3 \times 10^{-7}$ (see below) and $N = 10$. However, we found that a similar solution (ZB18a.N50, divergence time $\tau \simeq 58$ Ma to ZB18a) could be generated when raising J_2 by $\sim 0.3 \times 10^{-7}$ and N by 40[‡], where τ is the time when the maximum difference in Earth's eccentricity between two solutions irreversibly crosses $\sim 10\%$ of mean eccentricity ($\sim 0.028 \times 0.1$, see ref. 6 for details). Similar solutions could also be generated by lowering J_2 by $\sim 0.05 \times 10^{-7}$ and N by 5. In summary, certain combinations of J_2 and N lead to similar solutions, where similar here means $\tau \geq 58$ Ma to ZB18a.

It is important that J_2 and N changes of the order described above have a small overall effect on the solutions from 50-0 Ma because J_2 and N represent small terms. For comparison, if the Newtonian acceleration due to the Sun's mass at $r = 1$ au is order 1 ($GM/r^2 = 1$), then the J_2 term is $\sim GMJ_2R^2/r^4 \simeq 5 \times 10^{-12}$ and the contribution from a typical asteroid at 2 au distance $\sim Gm/2^2 \simeq 2.5 \times 10^{-11}$, where $R \simeq 0.00456$ au is the Sun's radius and $m = 1 \times 10^{-10}$ the asteroid mass in solar masses. As a result, e.g., ZB17c ($J_2 = 2.2 \times 10^{-7}, N = 10$) (6) and ZB18a.N50 ($J_2 = 1.6 \times 10^{-7}, N = 50$) agree up to $\tau \simeq 51$ Ma. However, changes in J_2 and N are

[‡]For $N = 50$, 10 asteroids were included in `HNBody` as heavyweight particles (HWP) and 40 asteroids as lightweight particles (LWP) to keep integration times manageable. HWPs are subject to the same, full interactions as the planets and Pluto. LWPs are dynamically equivalent to HWPs but self-gravity (LWP-LWP forces) is ignored; HWP-LWP interactions are included.

important for the critical interval 60-50 Ma and hence for the comparison to geologic data ([main manuscript](#)).

The J_2 value of 1.3×10^{-7} in ZB18a is lower than 2.2×10^{-7} used in our earlier work (6), which is based on recent evidence (45–49). However, as described above, J_2 can be increased with a larger asteroid population. We only tested up to $N = 50$, while current ephemerides may include $N > 300$, and in reality N may be $> 10^6$ with size > 1 km (though only a small fraction of this is dynamically relevant). Nevertheless, given that $N = 50$ corresponds to $J_2 \simeq 1.6 \times 10^{-7}$, perhaps $J_2 \simeq 1.8 - 2.0 \times 10^{-7}$ is possible with a larger asteroid population, yet still short of 2.2×10^{-7} (note also that 100-Myr integrations with large N are computationally still very expensive). Thus, in order to generate solutions such as ZB18a (in closest agreement with the geologic data, see [main manuscript](#)), it appears one needs parameter values that somewhat deviate from our best knowledge of the current solar system. One possible reason is that we are still missing some small but important processes in long-term integrations of the solar system. If so, these are unlikely the Lense-Thirring effect (50–52) or the mass loss of the Sun, which we have both tested and both turned out to be too small.[§] Interestingly, the La10c solution (33) with a small RMSD (see [main manuscript](#)) used the INPOP08 ephemeris (53), which is considered less accurate than more recent versions such as INPOP10 (54) used for La11 (55). Yet, La10c fits the geologic data much better than La11 (see Table 1, [main manuscript](#) and ref. 27). Again, a possible indication that parameters required for long-term integrations compatible with geologic observations of the past are not fully compatible with our best knowledge of the current solar system.

[§]We used 1.9×10^{41} kg m² s⁻¹ for the Sun’s angular momentum (45, 52) and for its mass loss $\dot{M}/M = -7 \times 10^{-14}$ y⁻¹ (ref. 41, though cf. ref. 11).

S7 Uncertainties from data vs. astronomical solutions; resonance transition

Measurement errors and parameter variations in data analyses often lead to uncertainties and variations in a predicted variable, say X , where the propagated uncertainty, say σ_X , somehow scales with input error or magnitude of parameter variation in a deterministic way. For example, X and σ_X might be monotonic, smooth functions of parameter p . Such a relationship usually allows meaningful application of basic statistical methods, Monte Carlo simulations, etc. However, simple relationships between p and X are generally not observed for parameter variations in chaotic systems, including orbital solutions of the solar system.

For example, as mentioned above, our solution ZB18a is part of a class of solutions generated using certain parameter combinations of J_2 and N . If we set $N = \text{const.}$ and only vary J_2 , the resultant solutions are very similar up to ~ 58 Ma for, e.g., $J_2 = [1.525 \ 1.550 \ 1.600] \times 10^{-7}$ ($N = 50$). As a result, their RMSD (as defined in Table 1) are all ~ 0.69 . However, at $J_2 = 1.675 \times 10^{-7}$, the RMSD jumps to 1.09. This is a typical expression of chaos, as small differences in initial conditions or other parameters can produce very large differences in the final outcome. In this case, the small increase in J_2 causes the solutions to diverge at ~ 53 Ma, leading to fundamentally different properties 58-53 Ma. This type of behavior (which motivated our grouping into different solution classes, see above) is obviously not amenable to simple statistical analysis. As a result, even large ensemble integrations of orbital solutions do not lead to error statistics for comparison with, e.g., the results of (35).

Given that classes of solutions exist in the interval 58-53 Ma (one of which is represented by ZB18a), finding other solution classes with the same orbital eccentricity for the Earth but a different $g_4 - g_3$ and $s_4 - s_3$ pattern appears unlikely within the parameter limits of our knowledge of the solar system. We examined over 80 solutions in the ZB18a class (58-53 Ma), all of which showed nearly identical eccentricity, $g_4 - g_3$, and $s_4 - s_3$ pattern. Conversely, we examined over 80 solutions

in non-ZB18a classes (58-53 Ma), none of which showed the eccentricity, $g_4 - g_3$, or $s_4 - s_3$ pattern of ZB18a. This result is consistent with our statement above, though not exhaustive, as the ratio of sample size to total solution classes (within parameter limits) is unknown.

Importantly, the transition in $g_4 - g_3$ causes changes in the very long eccentricity nodes, which is a macroscopic feature that can be observed in the geologic data (see [main manuscript](#) and refs. [7](#), [27](#)). In our solution ZB18a, the period associated with $g_4 - g_3$ switches from ~ 1.5 Myr to ~ 2.4 Myr around 50 Ma, consistent with the interpretation of strata that span this interval ([27](#)). If a switch in the $(g_4 - g_3) : (s_4 - s_3)$ ratio indicates a resonance transition (and conversely, constancy indicates absence), then the $g_4 - g_3$ switch also indicates a resonance transition unless $s_4 - s_3$ would switch simultaneously from ~ 0.75 Myr to ~ 1.2 Myr to keep the ratio constant. To the best of our knowledge, such a resonance behavior has never been proposed theoretically (e.g., [56](#), [57](#)); nor have we found any values as low as ~ 0.75 Myr for $s_4 - s_3$ at all in over 160 solar system integrations. One future task to perform if/when appropriate data for $s_4 - s_3$ becomes available is to check whether the resonance transitions from $\sim 1:1$ or a different ratio to $\sim 1:2$ around 50 Ma.

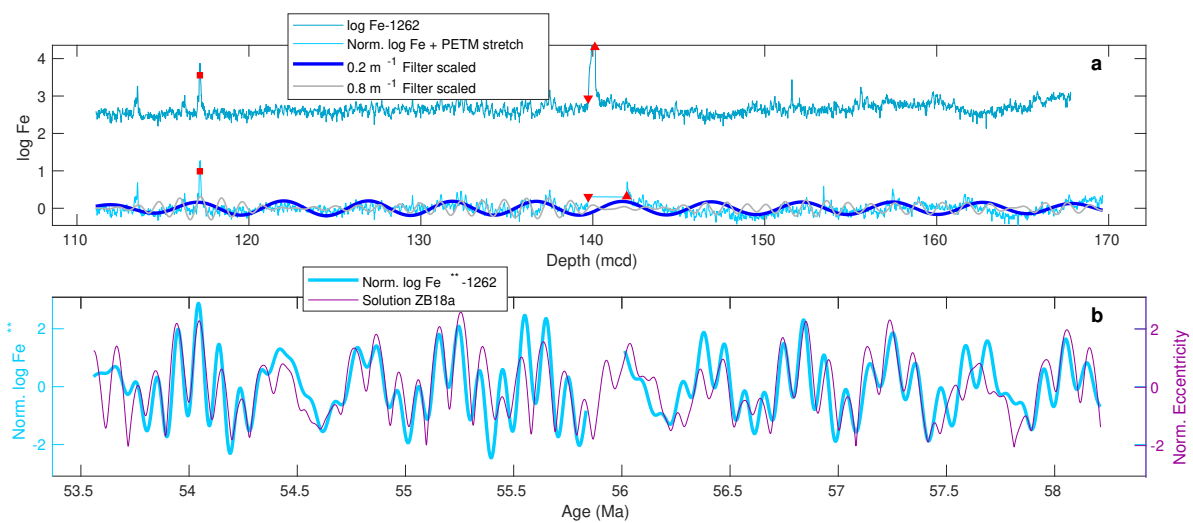


Figure S4. Final result of our analysis using iron intensity ($\log \text{Fe}$) (8, 58) (instead of color reflectance data a^*) at Ocean Drilling Program Site 1262, compared to our astronomical solution ZB18a. The two proxies (Fe and a^*) give nearly identical results; Fe^{**} is equivalent to a^{**} (cf. Fig. 1, main manuscript).

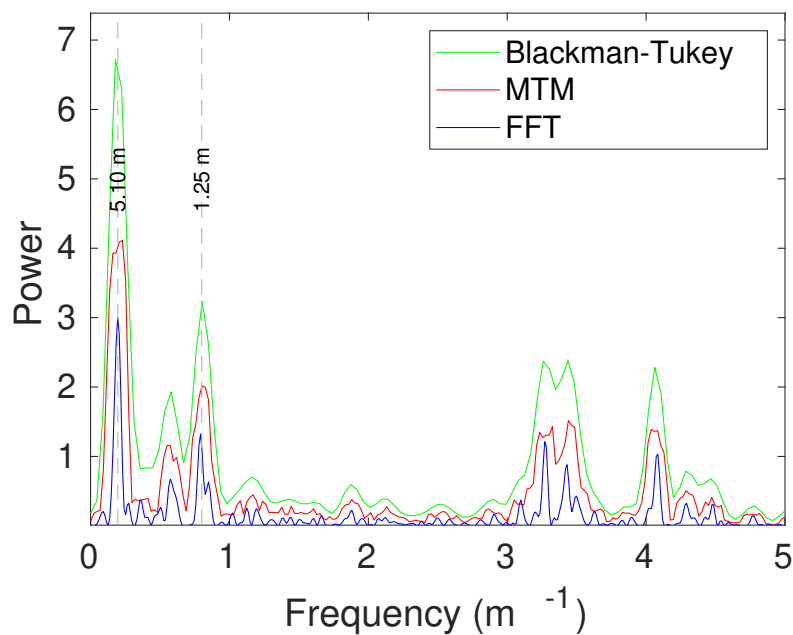


Figure S5. Spectra of a^* -1262 for the interval between (and excluding) PETM and ETM2 based on Blackman-Tukey (BT, 1/3 lag), multitaper method (MTM, time-bandwidth product $p = 2$, tapers = $2p - 1 = 3$), and Fast Fourier Transform (FFT). The cycles of ~ 5 m and ~ 1.25 m correspond to frequencies $f_1 \simeq 0.2 \text{ m}^{-1}$ and $f_2 \simeq 0.8 \text{ m}^{-1}$. Note that the small peak at $\sim 0.6 \text{ m}^{-1}$ is barely significant (95%) for the PETM-ETM2 interval and not significant for the full record. Using BT with 1/2 and 1/4 lag has no effect on f_1 and f_2 . Applying MTM with $p = 3$ changes f_1 and f_2 by $<0.009 \text{ m}^{-1}$ and $<0.0045 \text{ m}^{-1}$, respectively (zero-padding factor 5 and 10). Note that f_1 was refined *a posteriori* using the full ~ 5 -Myr record (see Methods).

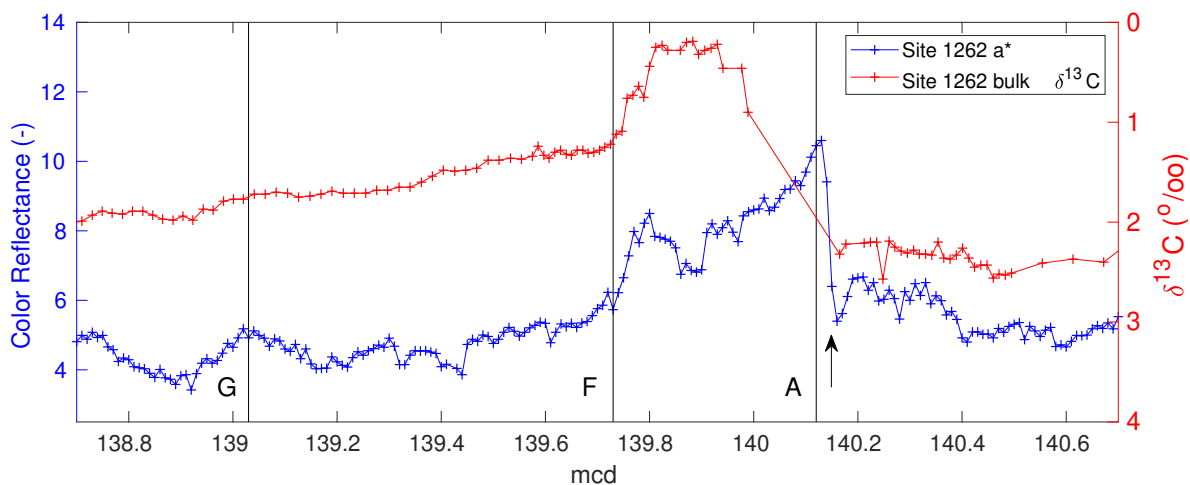


Figure S6. Color reflectance data (a^*) (7, 8) and bulk $\delta^{13}\text{C}$ at Ocean Drilling Program (ODP) Site 1262 across the PETM. Depth assignment of tie points (A, F, G) follows ref. 20. (A) PETM onset, located above rapid increase in a^* (arrow) at base of clay layer of Paleocene age (pre-PETM) due to erosion of CaCO_3 (22). (F) Recovery inflection point. (G) End of CIE recovery at ODP Site 690 (20). The time intervals A-F and A-G are denoted as t_{AF} and t_{AG} (see main manuscript). Sedimentation rates were reduced between A and F relative to pre-PETM levels but gradually increased to ~ 1.5 -2 times pre-PETM levels between F and G at Sites 1263 and 1266 (20, 21).

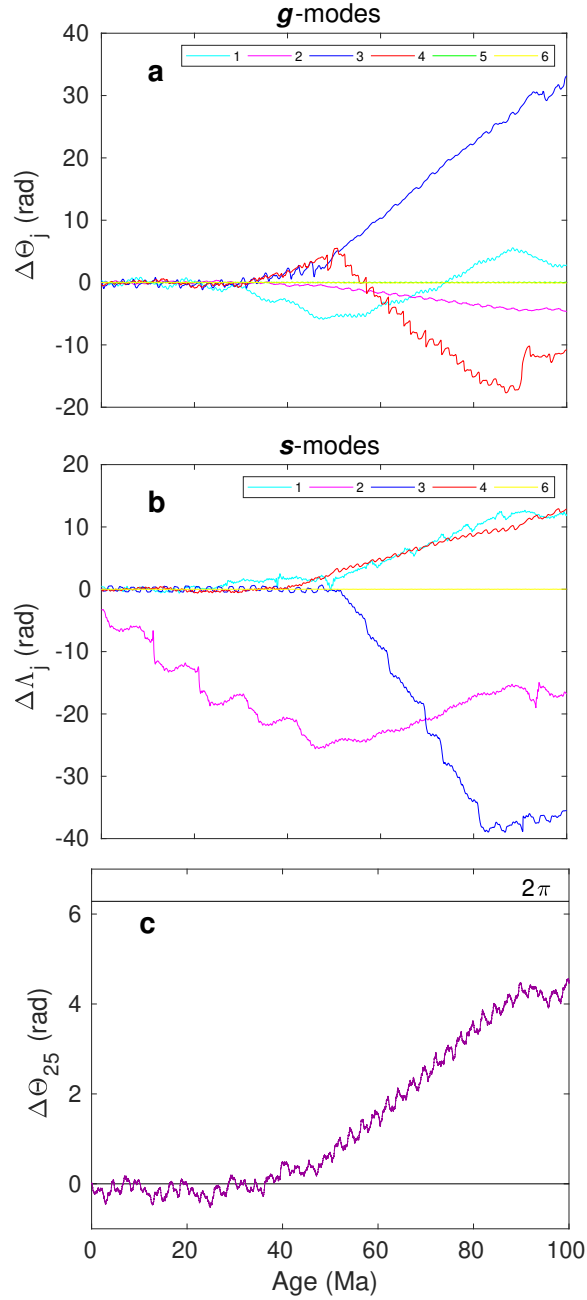


Figure S7. Differences in arguments (a) $\Delta\Theta_j = \Theta_j - \Theta_j^*$ and (b) $\Delta\Lambda_j = \Lambda_j - \Lambda_j^*$ (in radians) associated with g - and s -eigenmodes between the full numerical solution ZB18a (Θ_j, Λ_j) and a linear solution with constant frequencies (Θ_j^*, Λ_j^*) (see ref. 6 for details). Note the relatively rapid change in various arguments around 50 Ma (particularly for g_4 and s_3). (c) Difference in Θ_{25} of $g_2 - g_5 = g_{25}$ between ZB18a and constant g_{25} . $\Delta\Theta_{25} = 2\pi$ corresponds to a full period $P = 405$ kyr and hence the time offset between g_{25} in an astronomical solution and an age model that equates the long eccentricity cycle to exactly 405 kyr is $\Delta_t = P \cdot \Delta\Theta_{25}/2\pi$.

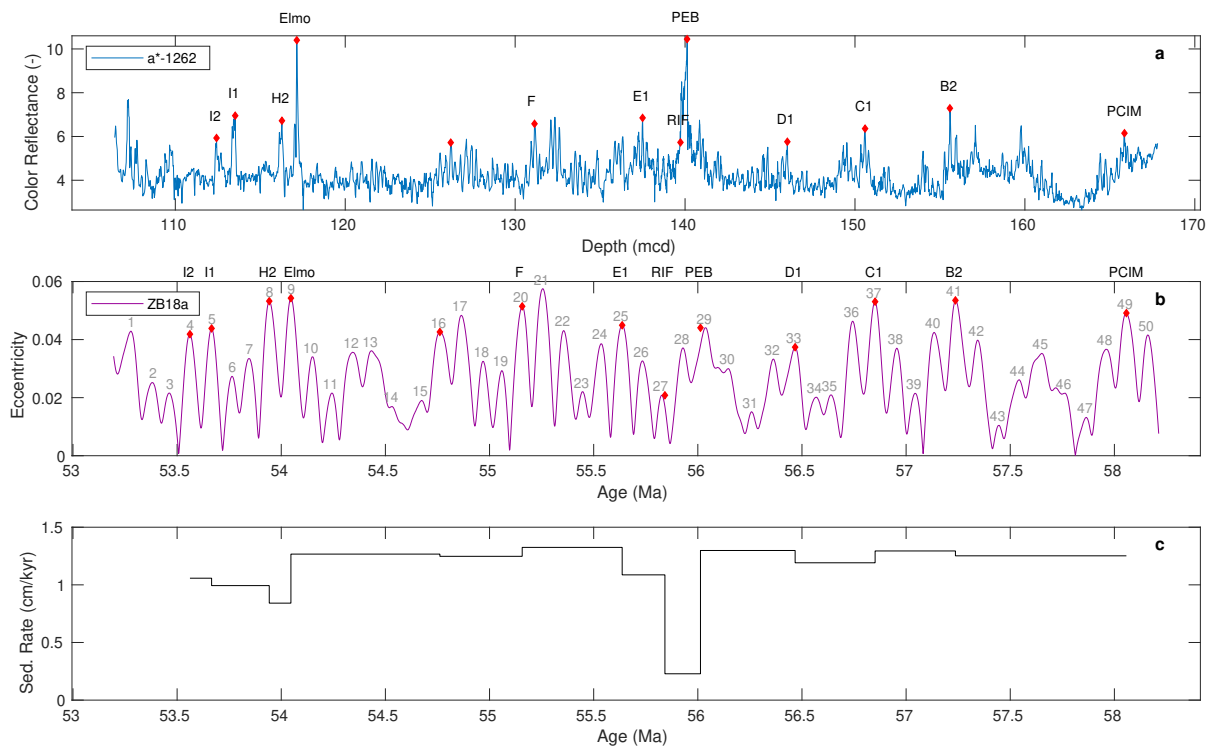


Figure S8. Astronomically calibrated age model for ODP Site 1262 based on ZB18a. (a) a^* record at Site 1262, red diamonds indicate tie points (for labels and ages, see Table S3); mcd = meters composite depth. (b) Our astronomical solution ZB18a. Numbers label maxima of short eccentricity cycles. Note that the P/E boundary (PEB) and recovery inflection point F (RIF, see Fig. S6) do not coincide with cycle maxima 29 and 27. (c) Inferred sedimentation rates for Site 1262.

Table S3. Tie points for astronomically calibrated age model at Site 1262 based on ZB18a.

Depth (mcd)	Age (Ma)	Events ^{a,b}
112.425	53.56	I2
113.525	53.67	I1
116.275	53.94	H2
117.150	54.05	Elmo
126.210	54.76	
131.140	55.16	F
137.500	55.64	E1
139.730	55.84	RIF
140.120	56.01	PEB
146.020	56.47	D1
150.595	56.85	C1
155.585	57.24	B2
165.860	58.06	PCIM

^aFor nomenclature, see refs. 27, 29, 59. RIF = Recovery Inflection point F (PETM, see Fig. S6). PEB = Paleocene-Eocene boundary.

PCIM = Paleocene Carbon Isotope Maximum.

^bSedimentation rates (r_{sed}) across and above Elmo are low (8, 10) (Fig. S8). Variable (vs. constant) r_{sed} hence adds one short cycle between H2 and I1. This has no effect on our PEB age and PETM duration (located below H2) and overall r_{sed} (main manuscript), as one cycle is added in depth and time domain.

References and Notes

1. H. Poincaré, *Les Méthodes Nouvelles de la Mécanique Céleste, Vol. 1* (Gauthier-Villars, 1892).
2. M. Milanković, *Kanon der Erdbestrahlung und Seine Anwendung auf das Eiszeitproblem* (Königl. Serb. Akad., 1941).
3. J. D. Hays, J. Imbrie, N. J. Shackleton, Variations in the Earth's Orbit: Pacemaker of the Ice Ages. *Science* **194**, 1121–1132 (1976). [doi:10.1126/science.194.4270.1121](https://doi.org/10.1126/science.194.4270.1121) [Medline](#)
4. F. Varadi, B. Runnegar, M. Ghil, Successive Refinements in Long-Term Integrations of Planetary Orbits. *Astrophys. J.* **592**, 620–630 (2003). [doi:10.1086/375560](https://doi.org/10.1086/375560)
5. J. Laskar, P. Robutel, F. Joutel, M. Gastineau, A. C. M. Correia, B. Levrard, A long-term numerical solution for the insolation quantities of the Earth. *Astron. Astrophys.* **428**, 261–285 (2004). [doi:10.1051/0004-6361:20041335](https://doi.org/10.1051/0004-6361:20041335)
6. R. E. Zeebe, Numerical Solutions for the Orbital Motion of the Solar System over the Past 100 Myr: Limits and New Results. *Astron. J.* **154**, 193 (2017). [doi:10.3847/1538-3881/aa8cce](https://doi.org/10.3847/1538-3881/aa8cce)
7. L. J. Lourens, A. Sluijs, D. Kroon, J. C. Zachos, E. Thomas, U. Röhl, J. Bowles, I. Raffi, Astronomical pacing of late Palaeocene to early Eocene global warming events. *Nature* **435**, 1083–1087 (2005). [doi:10.1038/nature03814](https://doi.org/10.1038/nature03814) [Medline](#)
8. T. Westerhold, U. Röhl, J. Laskar, I. Raffi, J. Bowles, L. J. Lourens, J. C. Zachos, On the duration of magnetochrons C24r and C25n and the timing of early Eocene global warming events: Implications from the Ocean Drilling Program Leg 208 Walvis Ridge depth transect. *Paleoceanogr. Paleoclimatol.* **22**, 2201 (2007). [doi:10.1029/2006PA001322](https://doi.org/10.1029/2006PA001322)
9. C. Ma, S. R. Meyers, B. B. Sageman, Theory of chaotic orbital variations confirmed by Cretaceous geological evidence. *Nature* **542**, 468–470 (2017). [doi:10.1038/nature21402](https://doi.org/10.1038/nature21402) [Medline](#)
10. M. Li, L. R. Kump, L. A. Hinnov, M. E. Mann, Tracking variable sedimentation rates and astronomical forcing in Phanerozoic paleoclimate proxy series with evolutionary correlation coefficients and hypothesis testing. *Earth Planet. Sci. Lett.* **501**, 165–179 (2018). [doi:10.1016/j.epsl.2018.08.041](https://doi.org/10.1016/j.epsl.2018.08.041)
11. C. Spalding, W. W. Fischer, G. Laughlin, An Orbital Window into the Ancient Sun's Mass. *Astrophys. J.* **869**, L17 (2018).
12. A. Morbidelli, *Modern Celestial Mechanics: Aspects of Solar System Dynamics* (Taylor & Francis, 2002).
13. J. Laskar, M. Gastineau, J.-B. Delisle, A. Farrés, A. Fienga, Strong chaos induced by close encounters with Ceres and Vesta. *Astron. Astrophys.* **532**, L4 (2011). [doi:10.1051/0004-6361/201117504](https://doi.org/10.1051/0004-6361/201117504)
14. S. R. Meyers, The evaluation of eccentricity-related amplitude modulation and bundling in paleoclimate data: An inverse approach for astrochronologic testing and time scale optimization. *Paleoceanogr. Paleoclimatol.* **30**, 1625–1640 (2015). [doi:10.1002/2015PA002850](https://doi.org/10.1002/2015PA002850)

15. S. R. Meyers, Cyclostratigraphy and the problem of astrochronologic testing. *Earth Sci. Rev.* **190**, 190–223 (2018). [doi:10.1016/j.earscirev.2018.11.015](https://doi.org/10.1016/j.earscirev.2018.11.015)
16. J. C. Zachos, U. Röhl, S. A. Schellenberg, A. Sluijs, D. A. Hodell, D. C. Kelly, E. Thomas, M. Nicolo, I. Raffi, L. J. Lourens, H. McCarren, D. Kroon, Rapid acidification of the ocean during the Paleocene-Eocene thermal maximum. *Science* **308**, 1611–1615 (2005). [doi:10.1126/science.1109004](https://doi.org/10.1126/science.1109004) [Medline](#)
17. Intergovernmental Panel on Climate Change, T. F. Stocker, et al., Eds., *Climate Change 2013: The Physical Science Basis* (Cambridge Univ. Press, 2013).
18. R. E. Zeebe, A. Ridgwell, J. Z. Zachos, Anthropogenic carbon release rate unprecedented during the past 66 million years. *Nat. Geosci.* **9**, 325–329 (2016). [doi:10.1038/ngeo2681](https://doi.org/10.1038/ngeo2681)
19. F. A. McInerney, S. L. Wing, The Paleocene-Eocene Thermal Maximum: A Perturbation of Carbon Cycle, Climate, and Biosphere with Implications for the Future. *Annu. Rev. Earth Planet. Sci.* **39**, 489–516 (2011). [doi:10.1146/annurev-earth-040610-133431](https://doi.org/10.1146/annurev-earth-040610-133431)
20. U. Röhl, T. Westerhold, T. J. Bralower, J. C. Zachos, On the duration of the Paleocene-Eocene thermal maximum (PETM). *Geochem. Geophys. Geosyst.* **8**, Q12002 (2007). [doi:10.1029/2007GC001784](https://doi.org/10.1029/2007GC001784)
21. B. H. Murphy, K. A. Farley, J. C. Zachos, An extraterrestrial ³He-based timescale for the Paleocene–Eocene thermal maximum (PETM) from Walvis Ridge, IODP Site 1266. *Geochim. Cosmochim. Acta* **74**, 5098–5108 (2010). [doi:10.1016/j.gca.2010.03.039](https://doi.org/10.1016/j.gca.2010.03.039)
22. R. E. Zeebe, J. C. Zachos, Reversed deep-sea carbonate ion basin gradient during Paleocene-Eocene thermal maximum. *Paleoceanogr. Paleoclimatol.* **22**, PA3201 (2007). [doi:10.1029/2006PA001395](https://doi.org/10.1029/2006PA001395)
23. R. E. Zeebe, Dynamic stability of the solar system: statistically inconclusive results from ensemble integrations. *Astrophys. J.* **798**, 8 (2015a). [doi:10.1088/0004-637X/798/1/8](https://doi.org/10.1088/0004-637X/798/1/8)
24. R. E. Zeebe, Highly stable evolution of earth’s future orbit despite chaotic behavior of the solar system. *Astrophys. J.* **811**, 9 (2015b). [doi:10.1088/0004-637X/811/1/9](https://doi.org/10.1088/0004-637X/811/1/9)
25. C. Jaramillo, D. Ochoa, L. Contreras, M. Pagani, H. Carvajal-Ortiz, L. M. Pratt, S. Krishnan, A. Cardona, M. Romero, L. Quiroz, G. Rodriguez, M. J. Rueda, F. de la Parra, S. Morón, W. Green, G. Bayona, C. Montes, O. Quintero, R. Ramirez, G. Mora, S. Schouten, H. Bermudez, R. Navarrete, F. Parra, M. Alvarán, J. Osorno, J. L. Crowley, V. Valencia, J. Vervoort, Effects of rapid global warming at the Paleocene-Eocene boundary on neotropical vegetation. *Science* **330**, 957–961 (2010). [doi:10.1126/science.1193833](https://doi.org/10.1126/science.1193833) [Medline](#)
26. A. J. Charles, D. J. Condon, I. C. Hardin, H. Palike, J. E. A. Marshall, Y. Cui, L. Kump, I. W. Croudace, Constraints on the numerical age of the Paleocene-Eocene boundary. *Geochem. Geophys. Geosyst.* **12**, Q0AA17 (2011). [doi:10.1029/2010GC003426](https://doi.org/10.1029/2010GC003426)
27. T. Westerhold, U. Röhl, T. Frederichs, C. Agnini, I. Raffi, J. C. Zachos, R. H. Wilkens, Astronomical calibration of the Ypresian timescale: Implications for seafloor spreading rates and the chaotic behavior of the solar system? *Clim. Past* **13**, 1129–1152 (2017). [doi:10.5194/cp-13-1129-2017](https://doi.org/10.5194/cp-13-1129-2017)

28. F. J. Hilgen, K. F. Kuiper, L. J. Lourens, Evaluation of the astronomical time scale for the Paleocene and earliest Eocene. *Earth Planet. Sci. Lett.* **300**, 139–151 (2010). [doi:10.1016/j.epsl.2010.09.044](https://doi.org/10.1016/j.epsl.2010.09.044)
29. B. S. Cramer, J. D. Wright, D. V. Kent, M.-P. Aubry, Orbital climate forcing of $\delta^{13}\text{C}$ excursions in the late Paleocene-early Eocene (chrons C24n-C25n). *Paleoceanogr. Paleoclimatol.* **18**, 1097 (2003). [doi:10.1029/2003PA000909](https://doi.org/10.1029/2003PA000909)
30. J. C. Zachos, H. McCarren, B. Murphy, U. Röhl, T. Westerhold, Tempo and scale of late Paleocene and early Eocene carbon isotope cycles: Implications for the origin of hyperthermals. *Earth Planet. Sci. Lett.* **299**, 242–249 (2010). [doi:10.1016/j.epsl.2010.09.004](https://doi.org/10.1016/j.epsl.2010.09.004)
31. T. Dunkley Jones, H. R. Manners, M. Hoggett, S. Kirtland Turner, T. Westerhold, M. J. Leng, R. D. Pancost, A. Ridgwell, L. Alegret, R. Duller, S. T. Grimes, Dynamics of sediment flux to a bathyal continental margin section through the Paleocene–Eocene Thermal Maximum. *Clim. Past* **14**, 1035–1049 (2018). [doi:10.5194/cp-14-1035-2018](https://doi.org/10.5194/cp-14-1035-2018)
32. R. E. Zeebe, T. Westerhold, K. Littler, J. C. Zachos, Orbital forcing of the Paleocene and Eocene carbon cycle. *Paleoceanogr. Paleoclimatol.* **32**, 440–465 (2017). [doi:10.1002/2016PA003054](https://doi.org/10.1002/2016PA003054)
33. J. Laskar, A. Fienga, M. Gastineau, H. Manche, La2010: a new orbital solution for the long-term motion of the Earth. *Astron. Astrophys.* **532**, A89 (2011). [doi:10.1051/0004-6361/201116836](https://doi.org/10.1051/0004-6361/201116836)
34. M. Ghil, M. R. Allen, M. D. Dettinger, K. Ide, D. Kondrashov, M. E. Mann, A. W. Robertson, A. Saunders, Y. Tian, F. Varadi, P. Yiou, Advanced spectral methods for climatic time series. *Rev. Geophys.* **40**, 3-1–3-41 (2002). [doi:10.1029/2000RG000092](https://doi.org/10.1029/2000RG000092)
35. S. R. Meyers, A. Malinverno, Proterozoic Milankovitch cycles and the history of the solar system. *Proc. Natl. Acad. Sci. U.S.A.* **115**, 6363–6368 (2018). [doi:10.1073/pnas.1717689115](https://doi.org/10.1073/pnas.1717689115) [Medline](#)
36. Shipboard Scientific Party, “Leg 208 summary,” in J. C. Zachos, D. Kroon, P. Blum, P., et al., Eds., Proc. ODP, Init. Repts., 208: College Station, TX (Ocean Drilling Program, 2004), pp. 1–112; [doi:10.2973/odp.proc.ir.208.101.2004](https://doi.org/10.2973/odp.proc.ir.208.101.2004).
37. V. Lauretano, J. C. Zachos, L. J. Lourens, Orbitally Paced Carbon and Deep-Sea Temperature Changes at the Peak of the Early Eocene Climatic Optimum. *Paleoceanogr. Paleoclimatol.* **33**, 1050–1065 (2018). [doi:10.1029/2018PA003422](https://doi.org/10.1029/2018PA003422)
38. T. Westerhold, U. Röhl, B. Donner, J. C. Zachos, Global Extent of Early Eocene Hyperthermal Events: A New Pacific Benthic Foraminiferal Isotope Record From Shatsky Rise (ODP Site 1209). *Paleoceanogr. Paleoclimatol.* **33**, 626–642 (2018). [doi:10.1029/2017PA003306](https://doi.org/10.1029/2017PA003306)
39. K. P. Rauch, D. P. Hamilton, “The HNBODY package for symplectic integration of nearly-Keplerian systems,” in *American Astronomical Society, DDA Meeting #33, id.08.02; Bulletin of the American Astronomical Society* (American Astronomical Society, 2002), vol. 34, p. 938

40. J. Wisdom, M. Holman, Symplectic maps for the n-body problem. *Astron. J.* **102**, 1528 (1991). [doi:10.1086/115978](https://doi.org/10.1086/115978)
41. T. R. Quinn, S. Tremaine, M. Duncan, A three million year integration of the earth's orbit. *Astron. J.* **101**, 2287 (1991). [doi:10.1086/115850](https://doi.org/10.1086/115850)
42. W. M. Folkner, J. G. Williams, D. H. Boggs, R. S. Park, P. Kuchynka, *Interplanetary Network Progress Report* **196**, 1 (2014).
43. J. Laskar, A numerical experiment on the chaotic behaviour of the Solar System. *Nature* **338**, 237–238 (1989). [doi:10.1038/338237a0](https://doi.org/10.1038/338237a0)
44. C. Ma, S. R. Meyers, B. B. Sageman, Testing Late Cretaceous astronomical solutions in a 15 million year astrochronologic record from North America. *Earth Planet. Sci. Lett.* **513**, 1–11 (2019). [doi:10.1016/j.epsl.2019.01.053](https://doi.org/10.1016/j.epsl.2019.01.053)
45. F. P. Pijpers, Helioseismic determination of the solar gravitational quadrupole moment. *Mon. Not. R. Astron. Soc.* **297**, L76–L80 (1998). [doi:10.1046/j.1365-8711.1998.01801.x](https://doi.org/10.1046/j.1365-8711.1998.01801.x)
46. R. Mecheri, T. Abdelatif, A. Irbah, J. Provost, G. Berthomieu, New values of gravitational moments J_2 and J_4 deduced from helioseismology. *Sol. Phys.* **222**, 191–197 (2004). [doi:10.1023/B:SOLA.0000043563.96766.21](https://doi.org/10.1023/B:SOLA.0000043563.96766.21)
47. A. Fienga, J. Laskar, P. Exertier, H. Manche, M. Gastineau, Numerical estimation of the sensitivity of INPOP planetary ephemerides to general relativity parameters. *Celestial Mech. Dyn. Astron.* **123**, 325–349 (2015). [doi:10.1007/s10569-015-9639-y](https://doi.org/10.1007/s10569-015-9639-y)
48. E. V. Pitjeva, N. P. Pitjev, Development of planetary ephemerides EPM and their applications. *Celestial Mech. Dyn. Astron.* **119**, 237–256 (2014). [doi:10.1007/s10569-014-9569-0](https://doi.org/10.1007/s10569-014-9569-0)
49. R. S. Park, W. M. Folkner, A. S. Konopliv, J. G. Williams, D. E. Smith, M. T. Zuber, Precession of Mercury's Perihelion from Ranging to the *MESSENGER* Spacecraft. *Astron. J.* **153**, 121 (2017). [doi:10.3847/1538-3881/aa5be2](https://doi.org/10.3847/1538-3881/aa5be2)
50. J. Lense, H. Thirring, On the influence of the proper rotation of a central body on the motion of the planets and the moon, according to Einstein's theory of gravitation. *Phys. Z.* **19**, 156–163 (1918).
51. M. H. Soffel, *Relativity in Astrometry, Celestial Mechanics and Geodesy* (Springer, 1989).
52. L. Iorio, Is it possible to measure the Lense-Thirring effect on the orbits of the planets in the gravitational field of the Sun? *Astron. Astrophys.* **431**, 385–389 (2005). [doi:10.1051/0004-6361:20041646](https://doi.org/10.1051/0004-6361:20041646)
53. A. Fienga, J. Laskar, T. Morley, H. Manche, P. Kuchynka, C. Le Poncin-Lafitte, F. Budnik, M. Gastineau, L. Somenzi, INPOP08, a 4-D planetary ephemeris: From asteroid and time-scale computations to ESA Mars Express and Venus Express contributions. *Astron. Astrophys.* **507**, 1675–1686 (2009). [doi:10.1051/0004-6361/200911755](https://doi.org/10.1051/0004-6361/200911755)
54. A. Fienga, J. Laskar, P. Kuchynka, H. Manche, G. Desvignes, M. Gastineau, I. Cognard, G. Theureau, The INPOP10a planetary ephemeris and its applications in fundamental physics. *Celestial Mech. Dyn. Astron.* **111**, 363–385 (2011). [doi:10.1007/s10569-011-9377-8](https://doi.org/10.1007/s10569-011-9377-8)

55. T. Westerhold, U. Röhl, J. Laskar, Time scale controversy: Accurate orbital calibration of the early Paleogene. *Geochem. Geophys. Geosyst.* **13**, Q06015 (2012).
[doi:10.1029/2012GC004096](https://doi.org/10.1029/2012GC004096)
56. J. Laskar, The chaotic motion of the solar system: A numerical estimate of the size of the chaotic zones. *Icarus* **88**, 266–291 (1990). [doi:10.1016/0019-1035\(90\)90084-M](https://doi.org/10.1016/0019-1035(90)90084-M)
57. G. J. Sussman, J. Wisdom, Chaotic evolution of the solar system. *Science* **257**, 56–62 (1992).
[doi:10.1126/science.257.5066.56](https://doi.org/10.1126/science.257.5066.56) [Medline](#)
58. T. Westerhold, U. Röhl, I. Raffi, E. Fornaciari, S. Monechi, V. Reale, J. Bowles, H. F. Evans, Astronomical calibration of the Paleocene time. *Palaeogeogr. Palaeoclimatol. Palaeoecol.* **257**, 377–403 (2008). [doi:10.1016/j.palaeo.2007.09.016](https://doi.org/10.1016/j.palaeo.2007.09.016)
59. V. Lauretano, F. Hilgen, J. Zachos, L. Lourens, Astronomically tuned age model for the early Eocene carbon isotope events: A new high-resolution $\delta^{13}\text{C}_{\text{benthic}}$ record of ODP Site 1263 between ~49 and ~54 Ma. *Newsl. Stratigr.* **49**, 383–400 (2016).
[doi:10.1127/nos/2016/0077](https://doi.org/10.1127/nos/2016/0077)